

Inversion and uncertainty estimation of gravity data using simulated annealing: An application over Lake Vostok, East Antarctica

Lopamudra Roy¹, Mrinal K. Sen¹, Donald D. Blankenship¹,
Paul L. Stoffa¹, and Thomas G. Richter¹

ABSTRACT

Interpretation of gravity data warrants uncertainty estimation because of its inherent nonuniqueness. Although the uncertainties in model parameters cannot be completely reduced, they can aid in the meaningful interpretation of results. Here we have employed a simulated annealing (SA)-based technique in the inversion of gravity data to derive multilayered earth models consisting of two and three dimensional bodies. In our approach, we assume that the density contrast is known, and we solve for the coordinates or shapes of the causative bodies, resulting in a nonlinear inverse problem. We attempt to sample the model space extensively so as to estimate several equally likely models. We then use all the models sampled by SA to construct an approximate, marginal posterior probability density function (PPD) in model space and several orders of moments.

The correlation matrix clearly shows the interdependence of different model parameters and the corresponding trade-offs. Such correlation plots are used to study the effect of a priori information in reducing the uncertainty in the solutions. We also investigate the use of derivative information to obtain better depth resolution and to reduce underlying uncertainties.

We applied the technique on two synthetic data sets and an airborne-gravity data set collected over Lake Vostok, East Antarctica, for which a priori constraints were derived from available seismic and radar profiles. The inversion results produced depths of the lake in the survey area along with the thickness of sediments. The resulting uncertainties are interpreted in terms of the experimental geometry and data error.

INTRODUCTION

Gravity anomalies are generated by mass variations in subsurface rock layers. The aim of inversion of gravity anomalies is to estimate the densities and shapes (including depth) of the causative bodies. Ambiguity in gravity inversion is well known so that a significant trade-off exists between density and geometry. There are two general solution methods for the problem of inverse-gravity: linear and nonlinear. In a linear approach, the source is considered as an ensemble of a number of rectangular blocks of known geometries, e.g., rectangular, and the density of each block is to be determined. This approach is suitable when the density contrast is not known a priori and/or significant density variation exists within the source. To minimize or reduce the nonuniqueness problems, several constraints, such as minimum volume (Last and Kubik, 1983), minimum moment of inertia (Guillen and Menichetti, 1984), and minimum/maximum depth bounds, etc., are used to restrict the number of solutions and to reflect the actual geology of the area. Nagihara and Stuart (2001) solved the linear inverse problem to model a salt structure and used an SA-based technique for uncertainty analysis of the results. In the nonlinear approach, the density contrast of the source is assumed to be known, and the shape of the body is established by determining the positions of the corners of arbitrary-shaped polygons (Talwani et al., 1959; Talwani and Ewing, 1960), or by computing the thickness of rectangular prisms of equal width (Bott, 1960; Cordell and Henderson, 1968). In this case, the relation between the observed data and the unknown parameters is nonlinear.

The main problem with gravity is that gravity equations are ill posed, and are even more so as data coverage is reduced from a spherical surface to a truncated plane. To obtain geologically feasible models, equality or smoothness constraints on the depth of the interfaces (Barbosa et al., 1997) are commonly used. Leao et al. (1996) constrained gravity inversion by

Manuscript received by the Editor March 4, 2003; revised manuscript received July 8, 2004; published online January 14, 2005.

¹University of Texas at Austin, Institute for Geophysics, John A. and Katherine G. Jackson School of Geosciences, 4412 Spicewood Springs Road, Building 600, Austin, Texas 78759. E-mail: roylopalamudra@yahoo.com; mrinal@ig.utexas.edu.
© 2005 Society of Exploration Geophysicists. All rights reserved.

incorporating the knowledge of depths at some isolated points on the density interface. Use of all the above constraints can certainly reduce the number of models, but the inverted results may still be ambiguous for several reasons; namely, the noise present in the data, simplification of the forward model compared to the complexity of real earth geology, reliability of a priori information, etc. Therefore, instead of trying to present a single solution, we derive the uncertainties in the estimated results and present these in a quantitative manner. The uncertainty analysis results in a quantitative measure of the quality of the inversion result.

In our paper, we use a nonlinear approach to invert two- as well as three-dimensional gravity anomalies over two layered basins composed of water and sediment. The problem of estimating two interfaces separating three homogeneous media is an inherently nonunique problem. Thus, in the present work, we do not present the best-fit solution as a unique solution. We perform a statistical analysis using thousands of possible models. We use the very fast simulated annealing (VFSA) technique to invert the gravity anomaly. We use the large number of inverted models to construct a marginal posterior probability density function (PPD) and additional statistical measures, such as the mean, variance, and correlation, to analyze the uncertainty (Sen and Stoffa, 1996). In all the synthetic and field examples, the mean model is presented as the most probable and acceptable. We demonstrate our technique with application to two synthetic data sets and an airborne-gravity survey over Lake Vostok, East Antarctica.

METHODOLOGY

The first task of inversion is to formulate the forward problem in such a way that we can use maximum a priori information to restrict the models within the local geology. For two-dimensional inversions, we followed the method of Talwani et al. (1959) and modeled the basin with an n -cornered polygon (Figure 1a). The horizontal positions of the corners of the upper layer (water) coincide with those of the lower layer (sediment), and the vertical coordinates, or the depths of all the corners, are determined by data fitting. The depths of the corners of the upper layer are allowed to vary within a wide range, whereas for the lower layer, the lower limits are restricted by the depths of the upper limits at the corresponding points. The density contrasts between water and the basement and between sediment and the basement are assumed to be constant and known. Here, the basement is igneous rock with density values between 2.5 to 2.8 g/cm³. The gravity field at the i th observation point can be computed from the coordinates of each corner of the polygon and can be expressed as

$$g_i = \sum_{j=1}^K [F(x_j, z_{1j}) + F(x_j, z_{2j})], \quad (1)$$

where K is the total number of corners of the polygon, and $F(x_j, z_{1j})$ and $F(x_j, z_{2j})$ are the two nonlinear functions (Talwani et al., 1959) associated with the coordinates of the points defining the upper and lower layers, respectively.

For three-dimensional inversions, the basin is assumed to consist of a large number of elementary 3D prisms whose top surfaces are coincident with the reference plane (Figure 1b). The horizontal dimensions of all the prisms are known and are

restricted to a fixed value. These prisms make up the upper layer of the model. The lower layer is comprised of the same number of vertically adjacent prisms. The shallow surface of the lower layer is coincident with the deep surface of the upper layer. However, the depth of the deeper surface of the lower layer is allowed to vary. As the density contrasts of the layers with the host rock are assumed known, the only parameters to be estimated are the thicknesses of the prisms, which have a nonlinear relation with the gravity field given by

$$g_i = \sum_{j=1}^M f(u_j, r_i) + f(l_j, r_i), \quad i = 1, 2, \dots, N, \quad (2)$$

where M is the total number of vertical prisms for each layer, N is the number of observation points, $f(u_j, r_i)$ and $f(l_j, r_i)$ are nonlinear functions (Bott, 1960) associated with the i th gravity value caused by the prisms at the j th position, where u_j and l_j are the thickness of prisms defining the upper and lower layers, respectively, and r_i is the position vector of the i th observation point in x-y-z space.

We solve the nonlinear inverse problem to estimate z_1 and z_2 for equation 1 and u and l for equation 2 from the observed gravity data by minimizing a misfit function, which can be represented as

$$E = \omega_1 \varepsilon_1 + \omega_2 \varepsilon_2, \quad (3)$$

where

$$\varepsilon_1 = \frac{2 \sum (|g_{obs} - g_{cal}|)}{\sum (|g_{obs} - g_{cal}|) + \sum (|g_{obs} + g_{cal}|)}, \quad (4)$$

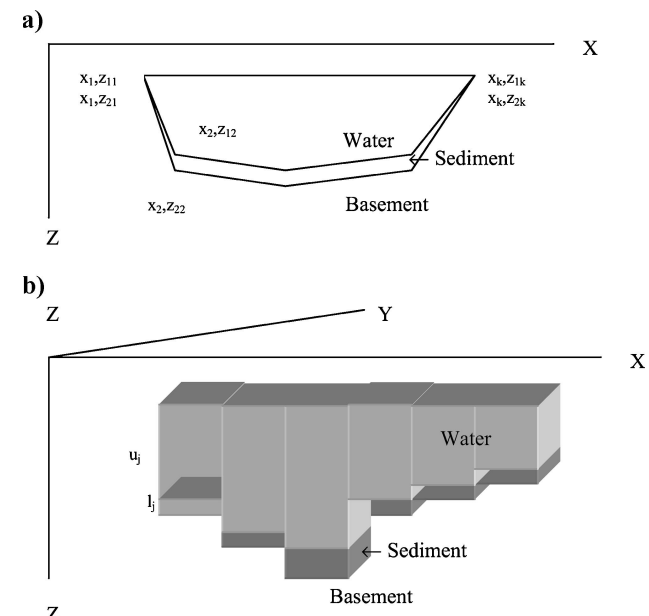


Figure 1. Schematic diagram of (a) 2D representation of the source body by n -cornered polygon and (b) 3D representation of the source volume by vertical rectangular prisms. In this application, our model consists of three layers, namely, the water, the sediment, and the basement.

and

$$\varepsilon_2 = \frac{2 \sum (|dg_{obs} - dg_{cal}|)}{\sum (|dg_{obs} - dg_{cal}|) + \sum (|dg_{obs} + dg_{cal}|)} . \quad (5)$$

Here, g stands for gravity anomaly, and dg is its derivative along the x, y, or z directions. For two-dimensional inversion, $(dg)^2 = (\partial g / \partial x)^2 + (\partial g / \partial z)^2$. For three-dimensional inversion, $(dg)^2 = (\partial g / \partial x)^2 + (\partial g / \partial y)^2 + (\partial g / \partial z)^2$. The summation is performed over all the data points. The numerator of equations 4 and 5 describes the closeness of the computed anomaly with the observed anomaly and with the corresponding derivatives, respectively. This absolute measure of misfit depends on the absolute magnitude of the anomaly, i.e., its value will be greater near the peak and less near the flanks of the anomaly. To avoid this bias, we normalized the misfit by multiplying it by a factor 2 and then dividing it by the denominator. The value of the misfit will now lie between 0.0 (when $g_{obs} = g_{cal}$) and 1.0 (when $|g_{obs} - g_{cal}|$ is infinite).

In mapping the interfaces, the weighting factors ω_1 and ω_2 depend on the relative importance of the gravity anomaly and its derivatives. The values of ω_1 and ω_2 are selected such that $\omega_1 + \omega_2 = 1$. For example, in the case of an intracratonic sag basin, for which the basement is essentially smooth, we can select zero or small values for ω_2 . On the other hand, for rifted basins having sharp discontinuities, ω_2 should be comparable to ω_1 . In Appendix A, using synthetic models, we explain how the derivatives of gravity anomalies of two different models can be different in spite of having almost the same gravity anomaly. Thus, if we use only ε_1 as the objective function, there will be several models that satisfy the observed gravity data equally well. But when we try to match the data and its derivatives, some models will be eliminated. In that sense, although ε_2 is not a stabilizing functional, it helps to reduce the uncertainties by reducing the number of possible models. Use of ε_2 does not reduce the inherent uncertainty, but it reduces the model uncertainty. We have used $\omega_1 = \omega_2 = 0.5$ when derivatives are used.

Simulated annealing

The basic concept of using SA as a strategy for optimization is derived from the process of annealing in thermodynamics (Kirkpatrick et al., 1983; Sen and Stoffa, 1995). The slow cooling of a molten material allows the reorientation of particles to form large crystals, whereas rapid cooling results in formation of glass. The former state is visualized as being equivalent to the global minimum of the energy of the system and the latter state to one of many possible local minima. During annealing, thermal equilibrium is reached at every temperature, and the probability of a particular configuration of particles being in state i , having energy governed by Boltzmann's distribution, is

$$p = \frac{\exp(-E_i/kT)}{\sum_{j \in S} \exp(-E_j/kT)}, \quad (6)$$

where E_i is the energy of state i , S represents the set of all possible configurations, k is the Boltzmann constant, and T is the temperature.

The SA technique starts with an initial model \mathbf{m}_0 , with associated error or energy $E(\mathbf{m}_0)$. It draws a new model \mathbf{m}_{new} from a flat distribution of models within the pre-defined limits. Note that each model parameter can be bounded by different limits. The associated energy (objective function value) $E(\mathbf{m}_{new})$ is then computed and compared to $E(\mathbf{m}_0)$. If the energy of the new state is less than the initial state, the new state is considered to be good. In this case, the new model is accepted and replaces the initial model unconditionally. However, if the energy of the new state is larger than the initial state, \mathbf{m}_{new} is accepted with the probability of $\exp\{-[E(\mathbf{m}_{new}) - E(\mathbf{m}_0)]/T\}$, where T is a control parameter called *annealing temperature*. This completes one iteration. It is the rule of accepting with a probability that makes it possible for SA to jump out of the local minima. The same process is repeated many times, with the annealing temperature gradually decreasing according to a predefined scheme. With a carefully defined cooling schedule, a global minimum can generally be found. One may choose a linear or a logarithmically decreasing cooling scheme. The trade-off here is between the computation cost and the accuracy of the result. Fast cooling will fail to produce a crystal (the algorithm gets trapped in a local minimum); slow cooling takes a long time but it will eventually find the global minimum.

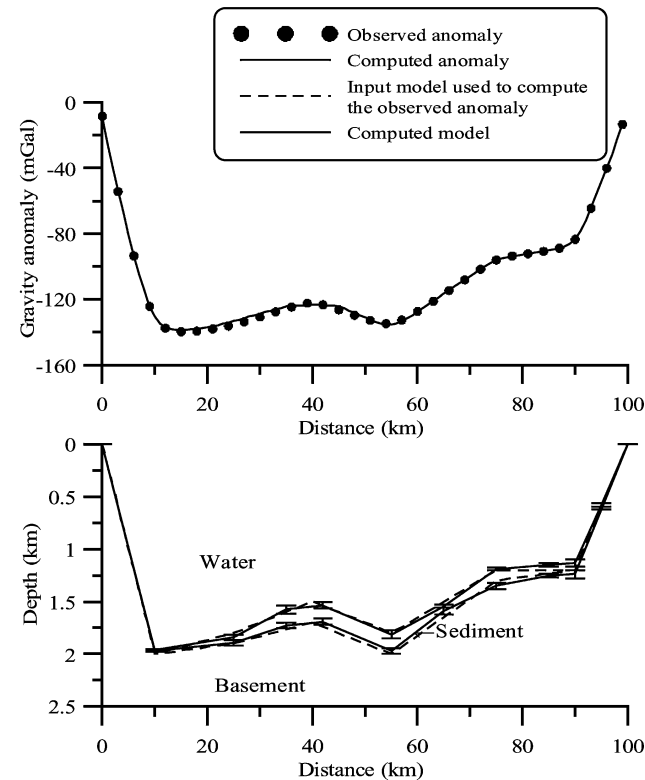
To speed up the annealing process with minimum sacrifice in the solution, a variant of SA, called very fast simulated annealing (VFSA) was proposed by Ingber (1989). VFSA differs from SA in the following ways: the new model is drawn from a temperature-dependent, Cauchy-like distribution centered on the current model. This change has two fundamental effects. First, it allows for larger sampling of the model space at early stages of the inversion, when the temperature is high, and much narrower sampling in the model space as the inversion converges, when the temperature decreases. Second, each model parameter can have its own cooling schedule and model space-sampling scheme, thereby allowing for individual control for each parameter and incorporation of a priori information. For many geophysical inversion applications, VFSA has performed very well (Sen and Stoffa, 1995).

The success of SA depends on proper selection of the initial temperature and cooling schedule. SA is best applied to the solution of a particular problem using different initial temperatures and cooling schedules. The most suitable control parameters are generally found after a few trials. In each iteration, the algorithm selects and evaluates a model chosen from within a predefined model space. We allow the algorithm to continue for several thousands of iterations, thus, we have several thousands of models having different misfits. Since our problem cannot have a unique solution, there is no real meaning to the best-fit model. Instead, using Bayesian statistics, we use all the models to construct an approximate marginal PPD function and several statistical measures, e.g., variance and correlation (Sen and Stoffa, 1996). These are discussed in detail in Appendix B. The moments are used to study underlying uncertainties; in other words, the degree of reliability of the inverted results. We use variance, a measure of spread about the mean, to represent the variability of each individual parameter. Correlation of one parameter with all other parameters reflects the ambiguities of interpretation. We use variance and correlation plots as judicial measurements to infer the reliability of a priori information and the quality of the interpreted result.

INVERSION AND UNCERTAINTY ESTIMATION USING SYNTHETIC DATA

We first test our methodology by inverting synthetic two-dimensional gravity data generated over a basin composed of

a)



b)

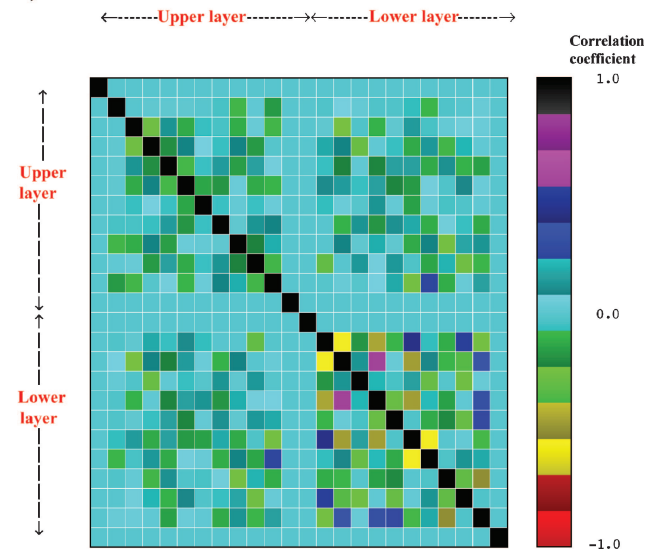
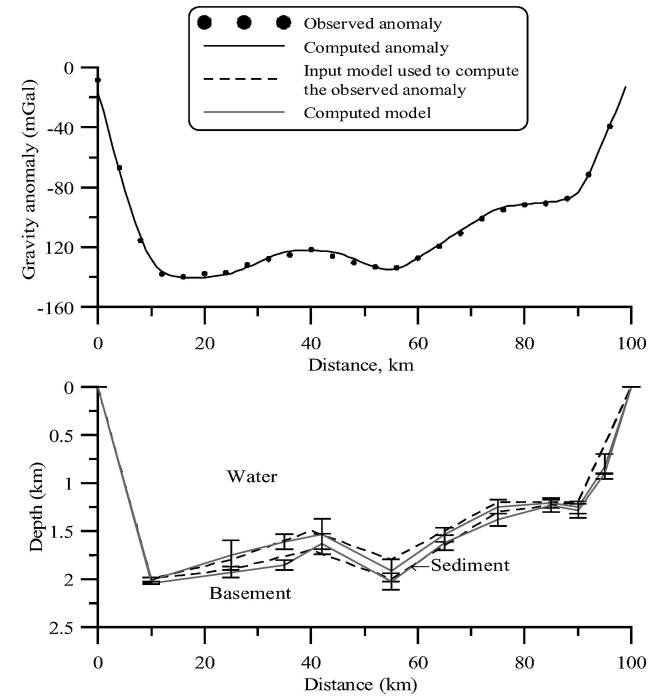


Figure 2. Inversion of noise-free synthetic data over a two-layered basin. (a) Observed and computed anomaly (top panel) and true and inverted model (bottom panel). Vertical bars show the variances at each depth point. To avoid clumsiness, we present the observed data as solid circles with a frequency less than the actual data. (b) Plot of correlation coefficients for each model parameter with all others. Note that most model parameters are fairly well resolved.

water and sediment (Figure 2a). The lateral extent of the lake is 100 km, and the sampling station interval is 1 km. We assume the density values of basement, sediment, and water to be 2.5 g/cm^3 , 2.0 g/cm^3 and 1.0 g/cm^3 , respectively (i.e., density contrast between water and basement is -1.5 g/cm^3 , and the contrast between sediment and basement is -0.5 g/cm^3). We construct the basin with a polygon having 12 corners for the upper layer (water body) and 24 corners for the lower layer (sediment), of which 12 corners coincide with the corners of the upper layers. Thus, there are 24 unknown depth values to be determined by inversion. We design our numerical

a)



b)

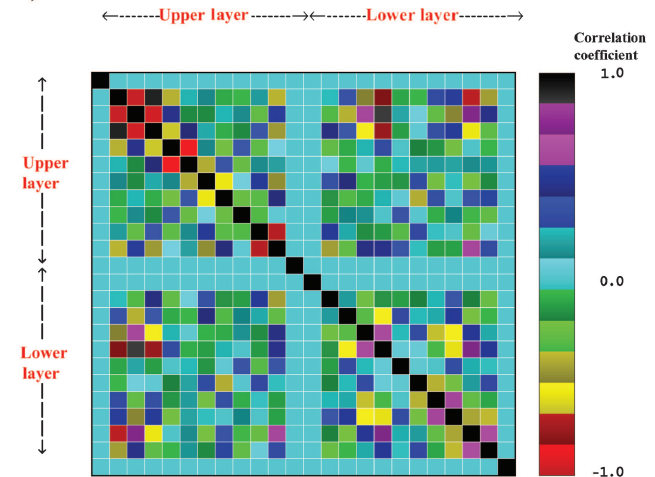


Figure 3. Inversion of synthetic data over a two-layered basin corrupted with 5% Gaussian noise. (a) Observed and computed anomaly (top panel) and true and inverted model (bottom panel). Vertical bars show the variances at each depth point. (b) Plot of correlation coefficients for each model parameter with all others. Note large correlation between different model parameters.

experiments to study (1) the effect of data noise and (2) the effect of incorrect prior information. We use the SA technique for thousands of iterations to invert the data, and thus get thousands of inverted models. First we invert the noise-free synthetic data using density values very close to the actual value. Obviously, the agreement of the inverted model (which is a mean model obtained from thousands of inverted models) with the true model and the computed data with the

observed data are nearly perfect (Figure 2a). The rms error between the observed and computed anomaly is 0.067 mGal. The depth values are very well determined, as evidenced by the small variances. Figure 2b shows the correlation plot. It is a matrix of 24 by 24 blocks, for which the diagonal elements are normalized to the value 1. For a unique result, there should be no significant correlation between different depth values, i.e., off-diagonal elements should be very small. Here, as the data are noise free and density contrasts are nearly exact, the correlation plot shows very low values in the off-diagonal elements, except for a few points. The correlation between different parameters is partly a result of the inherent nonuniqueness of the problem. Estimating two interfaces separating three homogeneous media can lead to nonunique solutions even for noise-free data with exact density values, the problem may not have a unique solution. By adjusting the depths of two layers, there can be several solutions satisfying the observed data equally well. This uncertainty increases with incorporation of noise and use of inappropriate a priori information.

Next, we corrupt the data with 5% uncorrelated Gaussian noise, but the density values remain the same. The inversion result (Figure 3a) shows that although the computed anomaly agrees well with the observed data (rms error is 0.17), some mismatches exist between the inverted and true models, and variances in the model parameters are generally large. The correlation plot (Figure 3b) shows several large off-diagonal values reflecting ambiguities in the result. The increase in uncertainty is caused by noise present in the data.

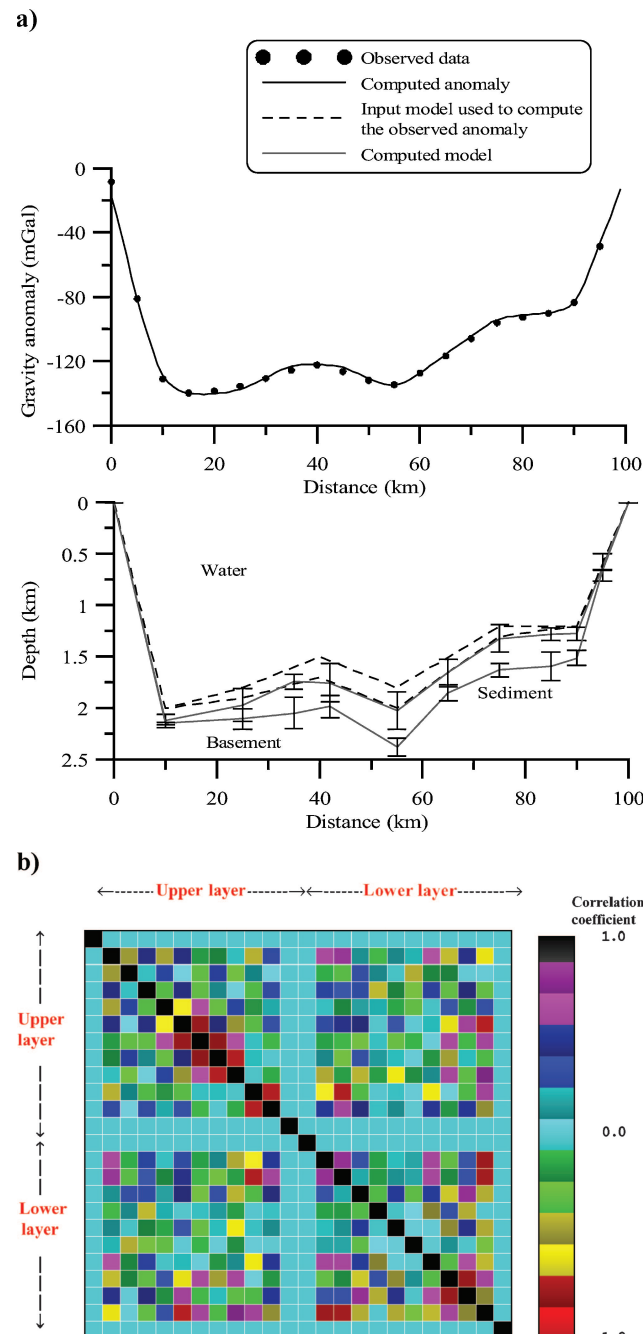


Figure 4. Inversion of noise-free synthetic data over a two-layered basin with incorrect a priori density contrasts. (a) Observed and computed anomaly (top panel) and true and inverted model (bottom panel). Vertical bars show the variances at each depth point. (b) Plot of correlation coefficients for each model parameter with all others.

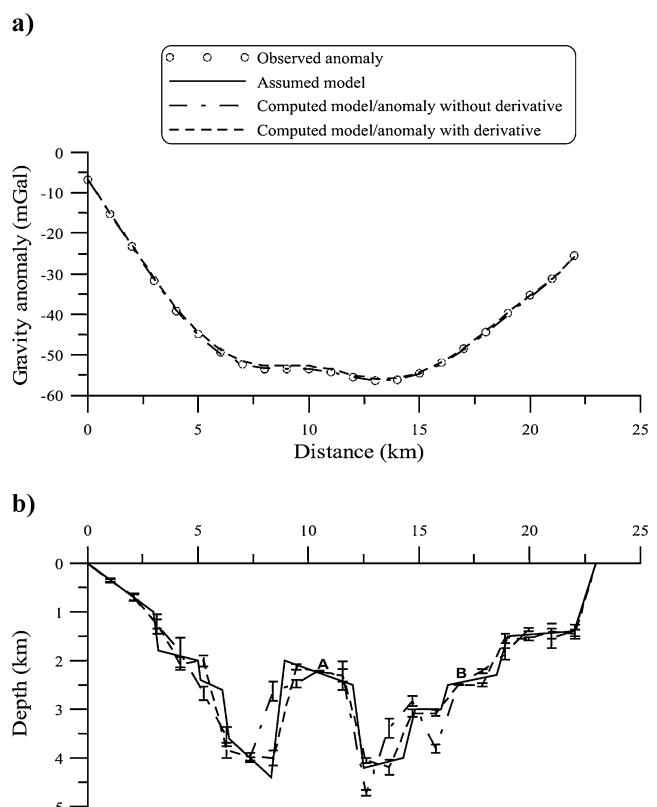


Figure 5. Comparison of results of inversion, performed over a synthetic data set from a rifted basin model, with and without using derivatives in the objective function. (a) Observed and computed anomalies and (b) the corresponding models.

To study the influence of a priori information on the uncertainty of the result, we deliberately used incorrect values for the density (2.4 g/cm^3 for the basement). We then inverted the noise-free data so that the outcome is primarily sensitive to a priori information. We find very good agreement between the observed and computed data (rms error 0.16), but the inverted mean model is very different from the true model. Note the high variability of depth values in Figure 4a. The correlation plot shows high positive as well as negative correlations among different depth values (Figure 4b). Comparison of the results from Figure 4 with those obtained for the actual density contrast (Figure 2) suggests that uncertainty analysis may be used to judge the quality of a priori information. For example, where the exact density values are not known, we can use several possible density values to invert the data and then examine their correlation functions for each density value. The plot showing minimum correlation will reflect the most probable density value.

Finally, we use a different synthetic model to study the effect of using derivative information in the objective function. The model is simulated on the basis of available geologic information for Malay Basin, Thailand. We selected this particular model to study the use of derivative information because the basin consists of several antithetic faults and an interbasinal ridge (Figure 5), and we want to show how the derivative information is useful in mapping these structural details. We assume the densities of the sediment and basement are 2.0 g/cm^3 and 2.5 g/cm^3 , respectively, so that the density contrast of sediment with bedrock is -0.5 g/cm^3 . Further, the depths at two isolated points A and B also are assumed to be known a priori. Initially, we use an objective function defined in equation 1 with $\omega_1 = 1.0$ and $\omega_2 = 0.0$. We find that even with an acceptable match between computed and observed anomalies (rms error 0.13), the inverted model is a smoother version of the real model. The variances in depths also are fairly large (Figure 5). To improve the result, we constrain the objective function by using the derivatives and use equal weights for ω_1 and ω_2 , i.e., $\omega_1 = \omega_2 = 0.5$. As the vertical and horizontal derivatives of gravity data form a Hilbert transform pair, we compute the vertical derivative by using the Hilbert transform of the horizontal derivatives. The inverted result considerably reduces the model mismatch as well as the variability of the depth values. The agreement between the observed and the computed anomaly also is improved (rms error 0.052). We now notice that the sharp changes in the model have been reproduced fairly well (Figure 5). It is important to note that measurements of gravity gradients are not made routinely. Here, we computed the gradients numerically for both the observed and computed data. The results from our synthetic example demonstrate that gradient

measurements, when available, would be very useful in constructing details of the model. In the absence of measured gradients, even a numerically computed gradient could be used to obtain better structural detail. In practice, the numerical gradients of field data generally contain high-frequency noise, which needs to be filtered out prior to use.

FIELD EXAMPLE—AN APPLICATION TO AIRBORNE GRAVITY DATA OVER LAKE VOSTOK, EAST ANTARCTICA

Lake Vostok is the earth's largest subglacial lake, located below a 4-km-thick ice sheet in the middle of East Antarctica (Siegert et al., 1996). The length of this wedge-shaped lake from north to south is about 300 km, and its width varies from 20 to 90 km (Kapista et al., 1996). The aerogeophysical data over the lake were acquired by the Institute for

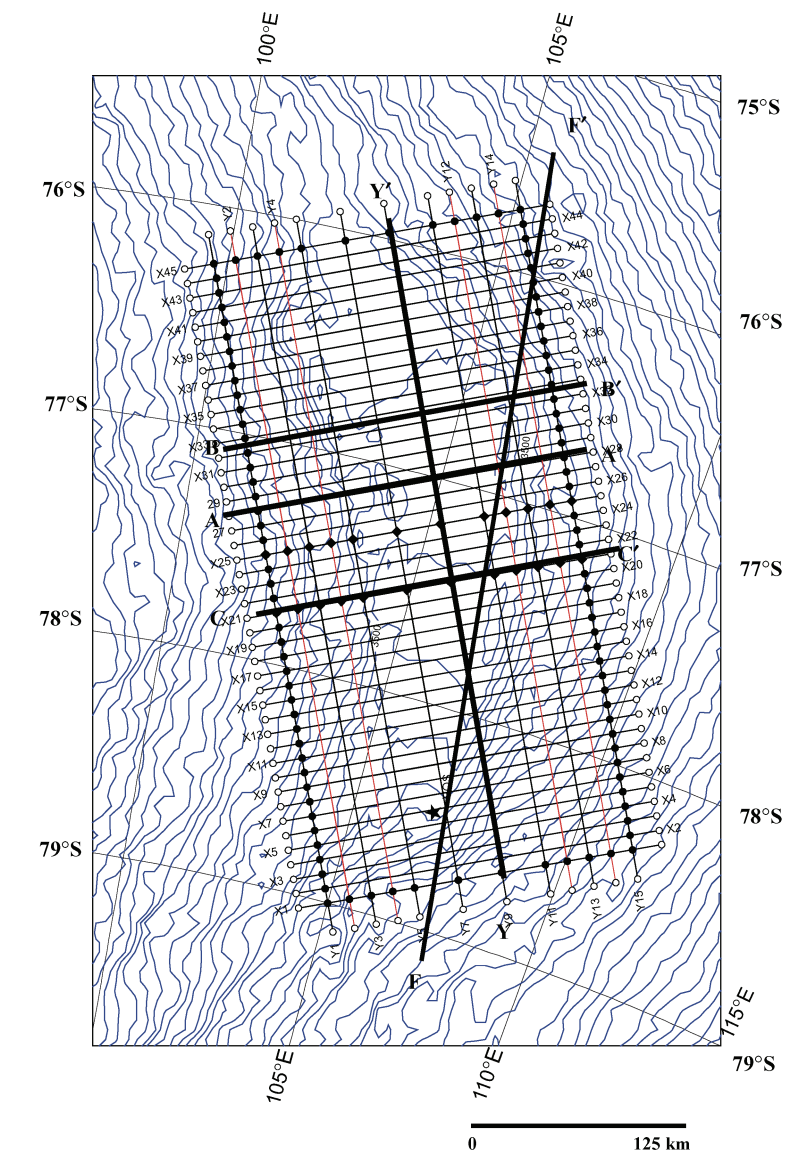


Figure 6. Survey area over Lake Vostok. AA', BB' and CC' are the profiles across the lake; YY' is the profile along the length of the lake; and FF' is a fault identified by Studinger et al. (2000). The contours represent surface topography.

Geophysics, University of Texas (UT) at Austin during 2000–2001. UT hired a De Havilland Twin Otter aircraft for this survey. The survey was performed using a Bell Aerospace BGM 3 gravimeter over a rectangular grid covering a 157.5- by 330-km area (Figure 6). The data were collected at a height of 500 to 1000 m above the ice sheet. Within the main grid, there are 45 flight lines, spaced 7.5-km apart. The average aircraft height was 3.96 km above mean sea level. Along with gravity data, laser altimetry and ice-penetrating–radar data also were acquired to map the ice-surface elevation and the ice thickness, respectively, over the area (Studinger et al., 2002). As with all airborne gravity surveys, numerous corrections and filters were applied to the data to reduce noise level and to enhance the actual gravity signal (Richter et al., 2001). The

accuracy of the corrected data is 1–2 mGal, and the spatial resolution of the estimated density is about 7.5 km (Richter et al., 2001). The gravity data were then reduced to mean sea level to obtain free-air gravity anomalies, which were reduced to Bouguer anomaly by using ice-penetrating radar information for the subice topography (radar cannot penetrate the water of the lake).

From the radar profiles of ice thickness, we know that the ice is present below mean sea level. Its total thickness is about 4 km, and its base varies from 0.4 to 0.8 km below mean sea level from south to north. In the present analysis, we consider ice and water as a single layer; thus, the ice-thickness information provides a constraint on the minimum depth of the first layer. Further, from the results of a seismic survey along a

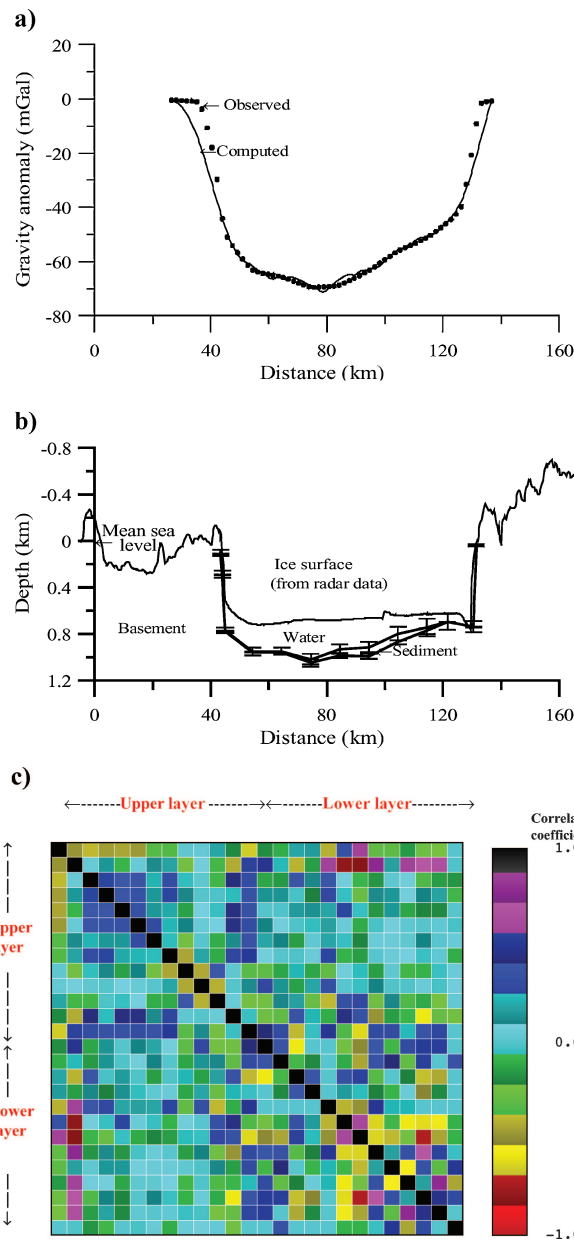


Figure 7. Results of inversion of gravity data along profile AA' of Lake Vostok without using constraints on water depth values. (a) Observed and computed anomaly, (b) corresponding model with variance at each depth point, and (c) correlation plot.

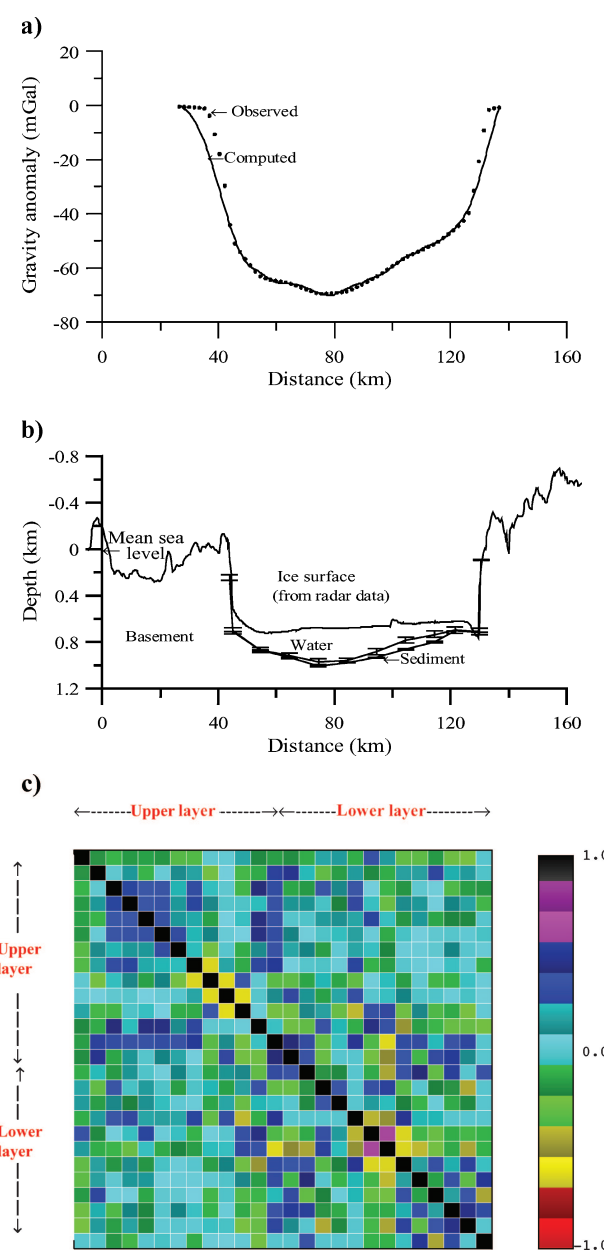


Figure 8. Results of inversion of gravity data along profile AA' of Lake Vostok using constrained water depth. (a) Observed and computed anomaly, (b) corresponding model with variance at each depth point, and (c) correlation plot.

few profiles over the lake (Masolov et al., 1999), we estimated the maximum water depth and sediment thickness. Our maximum search limit of water depth and sediment thickness is constrained by this information. (To avoid over-constraining the model, the maximum limit is fixed at nearly 1.3 times the maximum values obtained from the seismic survey.)

We first inverted several 2D gravity profiles over the lake. The results from the 2D inversion were used to constrain the search space in a more rigorous 3D inversion of the entire data set. The restricted or constrained search range reduces the computational time and accelerates convergence.

Inversion and uncertainty analysis: Results of 2D inversion

The density values of the water, sediment, and basement are considered to be 1.0, 2.0, and 2.7 g/cm³, respectively, so that the density contrast of water with bedrock is -1.7 g/cm³ and that of sediment with bedrock is -0.7 g/cm³. An east-west profile AA' (Figure 6) was inverted using simulated annealing. Initially, we use no constraints on the depth ranges and find that the agreement between the observed and the computed anomaly (Figure 7a) is quite good (rms error 0.22) and the mean model (Figure 7b) is consistent with the known geology. However, the variability of the depth values is large, and there are several high and low correlations between different depths (Figure 7c), indicating large uncertainties in the result. The same profile was inverted by constraining the minimum and maximum depths of the upper layer (from the radar and seismic survey information), resulting in a significant decrease in variances of the depth values (Figure 8b). The mismatch between the observed and computed anomaly also is reduced (rms error 0.096), as well as the correlations between different depth parameters (Figure 8c), which shows that the use of appropriate constraints can reduce the uncertainty.

Another profile, BB' (Figure 6), is selected to demonstrate the use of derivatives. This profile initially is inverted using the objective function defined in equation 1 with $\omega_1 = 1.0$ and $\omega_2 = 0.0$. Density values of different layers were considered the same as those used for profile AA'. We find satisfactory agreement between the observed and computed anomalies with an rms error of 0.088 (Figure 9a), whereas variances (presented as vertical bars in the figures) in depth values are moderate (Figure 9b). An inversion was repeated over the same profile by using $\omega_1 = \omega_2 = 0.5$, and the agreement between the observed and computed anomaly is found to be slightly better (Figure 10a) with an rms error of 0.072. Further, the inverted model resolves some high-frequency features, such as sharp corners (Figure 10b). This is the direct result of incorporating the derivative information. The plot of variance also indicates that the depth uncertainty is less compared to the inverted model shown in Figure 9b.

Inversion and uncertainty analysis: Results from 3D inversion

The data over the lake were averaged over an interval of 250 m along the profiles across the lake; the profiles were separated by 7.5 km.

The constraints used for the 3D inversion are:

- The lake boundary is constrained using the image of the lake obtained from ice penetrating radar data.

- The results from 2D inversion (which are performed over the entire lake using several 2D profiles) are used to restrict the lower and upper search limit of water depth and sediment thickness. Thus, for the 3D inversion, the search limit varies at different parts of the profile, while in the 2D inversion, we used the same search limit throughout.

Figure 11a shows the reduced gravity data, interpolated using a sampling interval of 2.6 km. Each observation point is

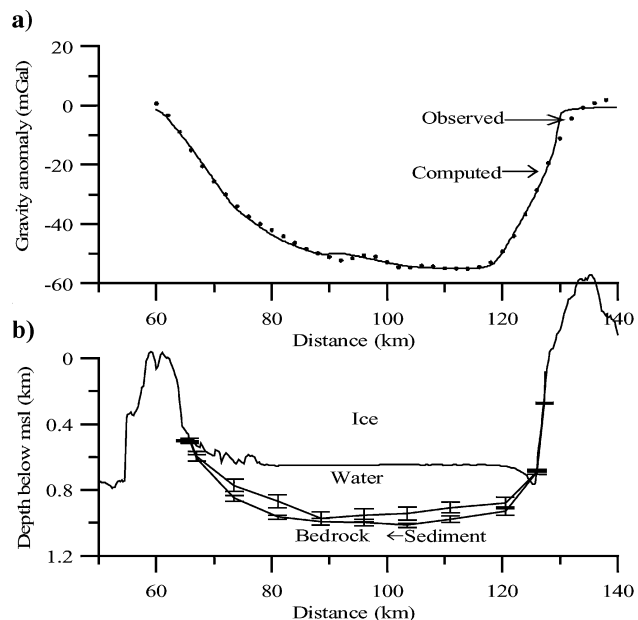


Figure 9. Results of inversion of gravity data along profile BB' of Lake Vostok without using derivative information in objective function. (a) Observed and computed anomaly and (b) corresponding model.

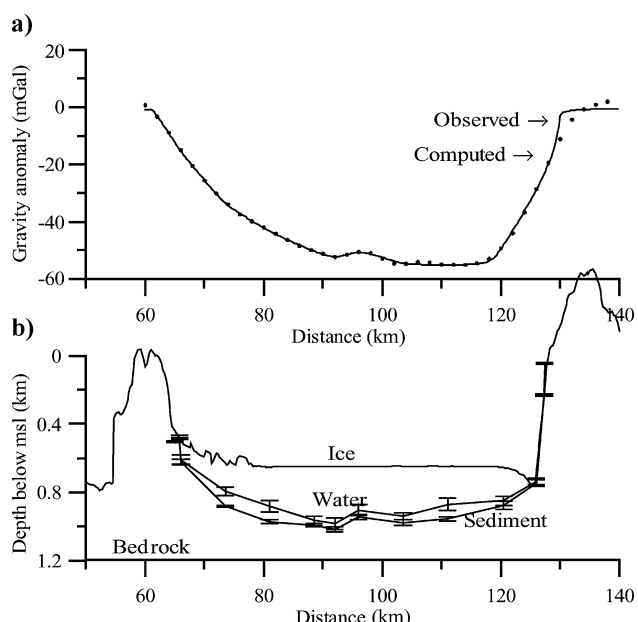


Figure 10. Results of inversion of gravity data along profile BB' of Lake Vostok using derivative information in objective function. (a) Observed and computed anomaly and (b) corresponding model.

associated with two vertically adjacent prisms, one for the upper layer (ice and water) and another for the lower layer (sediment). The total dimension of the model space is 100 by 50 by 2 blocks, and we invert the anomaly to obtain these 10,000 model parameters. Density values of water, sediment, and basement were initially considered to be 1.0 g/cm³, 2.0 g/cm³ and 2.7 g/cm³ respectively. Figure 11b shows the computed anomaly obtained from the inverted model without using any derivative information in the objective function. The water-column and sediment thicknesses are shown in Figures 11c and d, respectively. The plot of water-depth variance (Figure 11e) reveals that results along the edge of the basin, especially along the eastern boundary, are more ambiguous (or less certain), whereas anomalies below the lake bottom are fairly well determined. Further, we also observe that the steep gravity gradient at the edges of the observed anomaly is absent in the computed anomaly, i.e., the computed anomaly has a more flattened nature. We find three structural lows along the

lake axis. The low in the southern end is relatively shallow (nearly 1.0 km) and the middle and northern lows are as deep as 1.2 km. The seismic survey along the lake axis (Masolov et al., 1999) suggested only two deep zones, one at the southern end and the other at the middle. Maslow et al.'s interpretation suggested continuous thinning of the water layer toward the north. The disagreement of results can be attributed to the spatial sampling of the gravity data being finer than that of the seismic data. The station spacing of the seismic survey in the northern part is approximately 42 km (Masolov et al., 1999), whereas the diameter of the gravity-interpreted structural low is about 30–35 km.

To take care of the flattened nature of the computed gravity anomaly at the edges, we incorporated horizontal-gradient information in our objective function by using $\omega_1 = \omega_2 = 0.5$. From the interpretation obtained by Masolov et al. (1999) at the deepest part, the water depth is about 1.5 km, which is slightly more than what we obtained by inverting only the gravity anomalies (1.2 km). From the magnetic data over that area (Studinger et al., 2002), one can infer the existence of a sharp fault along the eastern boundary of the lake, with higher basement density to the east of the fault. We reinterpreted our data by constraining our model to a bedrock density value of 2.6 g/cm³ at the western side of the fault FF' (Figure 6) and 2.8 g/cm³ east of the fault. The results obtained using this new density distribution, as well as derivative information, show significant improvement in the computed anomaly (Figure 11f), as well as in edge uncertainties (Figure 11i). Since density is linearly related to the gravity anomaly, any change in density scales mostly the depth of the water body and sediment thickness. The new model assumes that the density of basement is less than 2.7 g/cm³ under most of the lake. Thus, although the basic structures of the mean models for water and sediment thickness (Figure 11g and h) are similar, the maximum depth of the water body and sediment thickness are greater in comparison to the previous result. The maximum water depth of the new model is about 1.55 km, which is now consistent with the seismic results. The improvement in anomaly mismatch at the edges mainly is a result of using derivative information. The difference between observed and computed (with derivative) anomalies is shown in Figure 11j. We observe that the mismatch is still high along the lake boundary, although the mismatch is less in the middle of the lake.

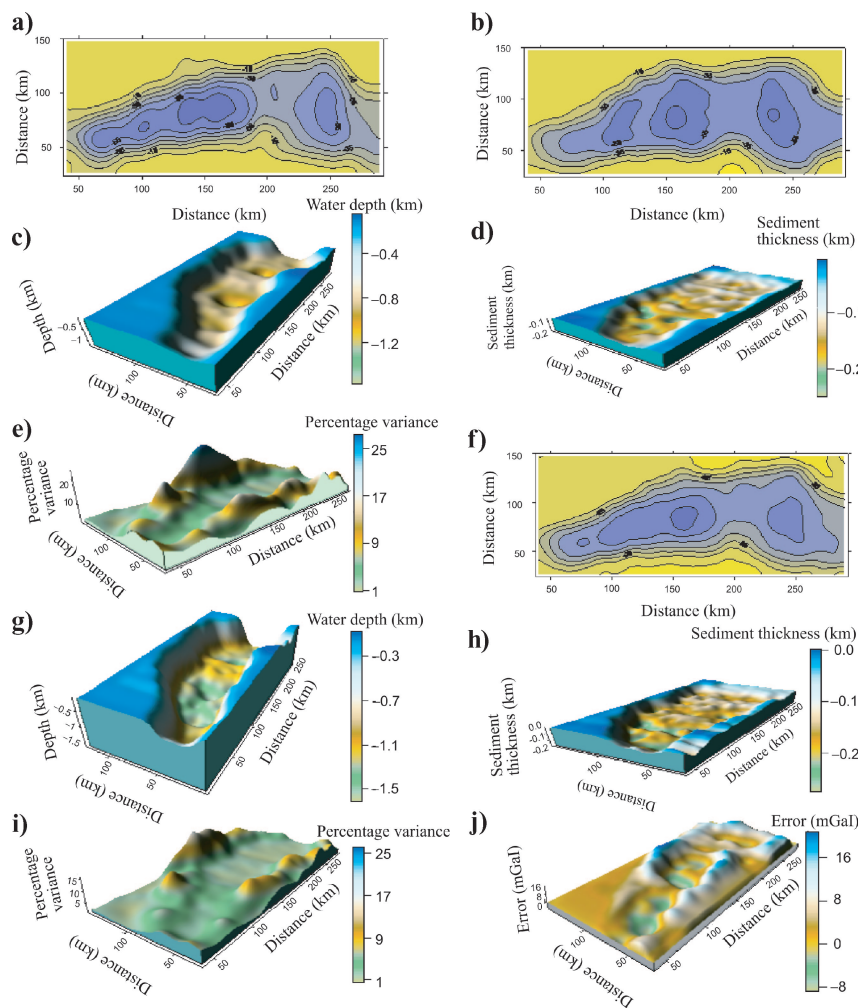


Figure 11. Results of 3D inversion of gravity data over Lake Vostok. (a) Observed data interpolated to a regular grid, (b) best-fit-computed anomaly without using derivative information in the objective function, (c) corresponding water depth and (d) sediment thickness, (e) normalized percentage variance of water depth, (f) computed anomaly using derivative information in the objective function, (g) corresponding water depth and (h) sediment thickness, (i) normalized percentage variance of water depth, and (j) difference between observed and computed (with derivative) anomaly. The contour interval in a, b, and f is 10 mGal.

Use of a marginal PPD function in uncertainty estimation

In all the above examples, we carried out several simulated annealing runs, starting with a model picked at random from the same search space. Each such run involved

several hundreds of iterations. During this process, we obtained thousands of inverted models and constructed the mean, variance, and correlation coefficients, which have been used to describe the quality of the result. Further, we constructed an approximate marginal PPD for each parameter based on the inverted models, following a method outlined by Sen and Stoffa (1996). The plot of the PPD (Figure 12a) along an east-west profile CC' (Figure 6) shows that at the beginning of the profile, as it is constrained by the lake shoreline from radar data, there is no spread in PPD value at all. We observe a wider spread of PPD values along the sharp edges of the lake in comparison to its bottom area. Figure 12b shows a plot of the PPD for each depth value along a profile YY' (Figure 6) running north-south through the middle of the lake. From these figures, it is clear that although the model space is quite wide (0 to 2 km), the PPD values die off quickly in most areas, i.e., the depth values are well constrained in those areas. The area of sharp change in lake depth is characterized by a broader PPD, which reveals the presence of more uncertainty over that region.

CONCLUSIONS

The present work is an attempt to estimate the underlying uncertainties in density models inverted from gravity data. The results of several studies, both synthetic and those based on actual field data, suggest that error analysis of any inversion does not reflect its limitation; instead, it strengthens the reliability of the results. In the current work, the uncertainties

in the results have been studied and presented in a statistical manner. By using several iterations of simulated annealing, we generated thousands of possible inverted models, selected from a predefined model space that is quite wide to allow the model to vary within a broad range. Several statistical measures of uncertainty, e.g., mean, variance, and correlation coefficients, were computed from inverted models. Judicial use of a correlation plot to select appropriate a priori information is shown for synthetic data. We further discussed the effects of constraints in reducing uncertainties. The use of derivatives in the objective function is also found to be useful in delineating in the models the sharp features, such as faulted edges. The derivative constraint also helped to improve agreement between observed and computed anomalies. The depth of the water body and sediment thickness obtained after using new density and derivative information is consistent with results from the seismic survey in the southern part of the lake.

The application of VFSA to 3D airborne gravity data over Lake Vostok demonstrates that we were able to delineate the basic structure of the bathymetry of the lake, which consists of three structural lows along its north-south axis. The maximum depth of the basement is about 1.5 to 1.6 km, whereas the sediment thickness varies between 50 and 300 m. The large variance along the lake boundary reflects the presence of large uncertainties along the edges, whereas very low variance over the lake bottom indicates that the bottom is quite well delineated. We present a plot of marginal PPD constructed over a profile along the major axes of the lake that clearly demonstrates that the lake bathymetry is well constrained.

The concepts and techniques presented here can be applied to other geologic areas. In the present work, we did not consider vertical variation of the density of the layers. For more complex geologic areas, the forward problem can be modified to handle the density-versus-depth function, and the same technique can be used. The application of our technique to gravity gradiometry or tensor-gravity data also is straightforward. However, the computation cost generally increases with the increase in the number of model parameters.

ACKNOWLEDGMENTS

This work was supported in part by National Science Foundation grant OPP-9911617. We would also like to express our appreciation to the personnel of the Support Office for Aerogeophysical Research (SOAR) at the University of Texas at Austin for their assistance in reduction of the Lake Vostok gravity data. These data were collected as the result of collaborative proposals by the University of Texas (principal investigators D. D. Blankenship, J. W. Holt, D. L. Morse, and I. W. Dalziel) and Columbia University (principal investigators R. E. Bell and M. Studinger). The fellowship of L. Roy is partially supported by a UTIG postdoctoral fellowship. The authors are thankful for the anonymous reviewers, the associate editor John Peirce, and the editor for their valuable suggestions that helped improve the clarity of this paper. This paper is The University of Texas Institute for Geophysics Contribution No. 1664.

APPENDIX A

Let us consider Figure A-1 to understand how derivatives can be used to reduce model uncertainty. Model 1 is a basin

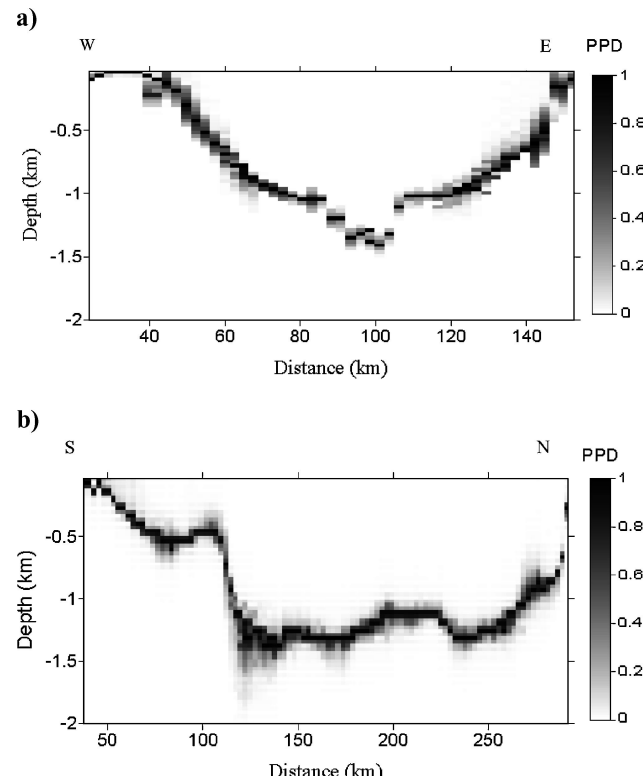


Figure 12. Plot of posterior probability density (PPD) for each depth point (a) over east-west profile CC' across the lake and (b) over north-south profile YY' along the lake.

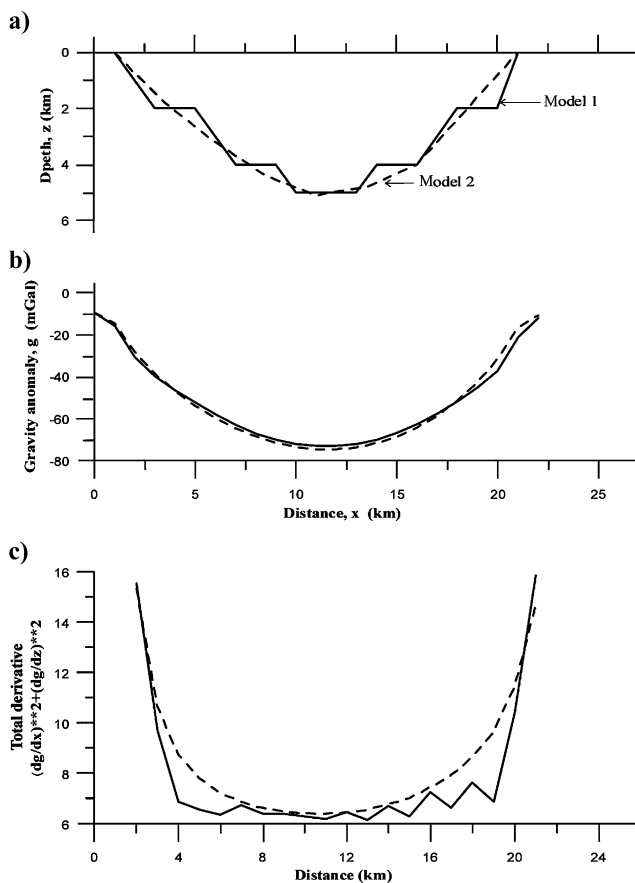


Figure A-1. Synthetic basin models. (a) Solid and dotted line represents the faulted and smooth basin, (b) corresponding gravity anomalies, and (c) corresponding derivatives.

having a smooth interface, and model 2 has several faults and steep edges (Figure A-1a). For the same density value of sediment and basement in both the basins, the gravity anomalies obtained are almost the same (Figure A-1b), although the models are different. Figure A-1c is a plot of the derivatives for the anomalies. It is clear that although the anomalies look the same, there are differences in the derivatives. Thus, while doing an inversion, minimization of the anomaly will give only a smoother version of the actual model. Use of the derivatives should prove useful in identifying some minute details of the model.

APPENDIX B

Tarantola (1987) formulated the inverse problem in a Bayesian framework in which the answer to an inverse problem is given in terms of a posterior probability density function (PPD), which is proportional to a product of a likelihood function and an a priori probability density function in model space. According to Bayes's theorem, derived from the definition of conditional probabilities, the PPD is defined as

$$\sigma(\mathbf{m}|\mathbf{d}_{obs}) \propto l(\mathbf{d}_{obs}|\mathbf{m})p(\mathbf{m}), \quad (B1)$$

where \mathbf{m} is a vector containing a set of parameter values; \mathbf{d}_{obs} is the data vector; $\sigma(\mathbf{m}|\mathbf{d}_{obs})$ is the PPD, which is the conditional

probability for each set of parameter values represented by vector \mathbf{m} given data in vector \mathbf{d}_{obs} ; $l(\mathbf{d}_{obs}|\mathbf{m})$ is the likelihood function expressing the conditional probability for the set of observations \mathbf{d}_{obs} given a set of parameter values \mathbf{m} ; and $p(\mathbf{m})$ is the “prior” probability for \mathbf{m} given expert judgment or other reasons to constrain the possible choices of \mathbf{m} independent of the observed data \mathbf{d}_{obs} . In our application, the likelihood function is expressed as

$$l(\mathbf{d}_{obs}|\mathbf{m}) \propto \exp[-E(\mathbf{m})], \quad (B2)$$

where $E(\mathbf{m})$ is the cost function defined in equation 3.

Once the PPD is known, the parameter means $\langle \mathbf{m} \rangle$ or covariances can be obtained through multidimensional integrals of the general form

$$\mathbf{I} = \int f(\mathbf{m})\sigma(\mathbf{m}|\mathbf{d}_{obs})d\mathbf{m}, \quad (B3)$$

where $f(\mathbf{m}) = \mathbf{m}$ for the parameter means or $f(\mathbf{m}) = (\mathbf{m} - \langle \mathbf{m} \rangle)(\mathbf{m} - \langle \mathbf{m} \rangle)^T$ for the parameter covariance matrix. Because the PPD is multidimensional, it is difficult to visualize. One approach is to display the marginal PPD, defined to be the one-dimensional projection of the multidimensional PPD [equivalent to setting $f(\mathbf{m}) = 1$ in equation B3 and integrating over all dimensions except for the dimension of interest].

The principal challenge to achieving our science goals is the computational expense of approximating the PPD. Much recent progress has been made on the theory and application of “importance” sampling as a way to improve upon the better-known methods for approximating the PPD, such as the “Grid search” or “Monte Carlo” approaches. The brute-force grid search and theoretically correct Gibbs’ sampling approach to evaluating the multidimensional integral given by equation (B3) are very compute-intensive. Sen and Stoffa (1996) proposed several inexpensive alternatives to the theoretically correct but compute-intensive approaches. In applications to several geophysical inverse problems they demonstrated that the multiple VFSA approach used here is the most efficient.

The VFSA algorithm, as presented by Ingber (1989) and used by Sen and Stoffa (1996), is an efficient method to identify optimal parameters, especially when nonlinearities are important. At the other extreme, a pure Monte Carlo or grid-search algorithm would provide the most accurate (nonbiased) map of the multidimensional PPD but may require more model evaluations than one can afford to make. Sen and Stoffa (1996) argue that one can slightly adapt the VFSA cooling schedule and convergence acceptance criterion, and allow for numerous repetitions of the minimization procedure to strike an efficient and effective balance between these two objectives. Depending on the application, one can save several orders of magnitude in the number of model evaluations over either the Monte Carlo or Grid-search algorithms (Sen and Stoffa 1996).

Sen and Stoffa (1996) demonstrated that the PPD derived through the VFSA search algorithm is unavoidably biased toward the peaks of the PPD because of the change in the temperature control parameter during the selection process of model parameters. However, the VFSA algorithm may be repeated a number of times with different starting models to allow sufficient sampling of the entire model space. This reduces the biases of the PPD and improves the estimates of

the model covariance matrix. While variances may be underestimated relative to what may be obtained through a theoretically correct Metropolis/Gibbs sampler, the normalized covariance matrix (the correlation matrix) has been found to be nearly equivalent between the two approaches (Sen and Stoffa 1996).

REFERENCES

- Barbosa, V. C. F., J. B. C. Silva, and W. E. Medeiros, 1997, Gravity inversion of basement relief using approximate equality constraints on depths: *Geophysics*, **62**, 1745–1757.
- Bott, M. H. P., 1960, The use of rapid digital computing methods for gravity interpretation of a sedimentary basin: *Geophysical Journal of the Royal Astronomical Society*, **3**, 63–67.
- Cordell, L., and R. G. Henderson, 1968, Iterative three dimensional solution of gravity anomaly data using a digital computer: *Geophysics*, **33**, 596–601.
- Guillen, A., and V. Menichetti, 1984, Gravity and magnetic inversion with minimization of a specific functional: *Geophysics*, **49**, 1354–1360.
- Ingber, L., 1989, Very fast simulated re-annealing: *Journal of Mathematical and Computer Modelling*, **12**, 967–973.
- Kapista, A. P., J. K. Ridley, G. de Q. Robin, M. J. Siegert, and I. A. Zotikov, 1996, A large deep fresh water lake beneath the ice of central East Antarctica: *Nature*, **381**, 684–686.
- Kirkpatrick, S. G., C. D. Delatt Jr. and M. P. Vecchi, 1983, Optimization by simulated annealing: *Science*, **220**, 671–680.
- Last, B. J., and K. Kubik, 1983, Compact gravity inversion: *Geophysics*, **46**, 713–721.
- Leao, J. W. D., P. T. L. Menezes, J. F. Beltrao, and J. B. C. Silva, 1996, Gravity inversion of basement relief constrained by knowledge of depth at isolated points: *Geophysics*, **61**, 1702–1714.
- Masolov, V. N., G. A. Kudryavtsev, and G. L. Leitchenkov, 1999, Earth science studies in the Lake Vostok Region: Existing data and proposal for future research: Presented at the Scientific Committee on Antarctic Research (SCAR) International Workshop on Subglacial Lake Exploration.
- Nagihara, S., and A. H. Stuart, 2001, Three dimensional gravity inversion using simulated annealing: Constraints on the diapiric roots of allochthonous salt structures: *Geophysics*, **66**, 1438–1449.
- Richter, T. G., J. W. Holt, and D. D. Blankenship, 2001, Air-borne gravity over East Antarctica: Proceedings of the International Symposium on Kinematic Systems in Geodesy, Geomatics and Navigation, Alberta, 576–585.
- Sen, M. K., and P. L. Stoffa, 1995, Global optimization methods in geophysical inversion: Elsevier Science Publ.
- Sen, M. K., and P. L. Stoffa, 1996, Bayesian inference, Gibbs' sampler and uncertainty estimation in geophysical inversion: *Geophysical Prospecting*, **44**, 313–350.
- Siegert, M. J., J. A. Dowdeswell, M. R. Gorman, and N. F. McIntyre, 1996, An inventory of Antarctic sub-glacial lakes: *Antarctic Science*, **8**, 281–286.
- Studinger, M., R. E. Bell, G. D. Karner, A. A. Tikku, J. W. Holt, D. L. Morse, and T. G. Richter et al., 2002, Ice flow, landscape setting and geological framework of Lake Vostok, East Antarctica: *Earth and Planetary Science Letters*, **205**, 195–210.
- Tarantola, A., 1987, Inverse problem theory: Methods of data fitting and model parameter estimation: Elsevier Science Publ.
- Talwani, M., J. L. Worzel, and M. Landisman, 1959, Rapid gravity computations for two-dimensional bodies with application to the Mendocino submarine fracture zone: *Journal of Geophysical Research*, **64**, 49–59.
- Talwani, M., and M. Ewing, 1960, Rapid computation of gravitational attraction of three dimensional bodies of arbitrary shape: *Geophysics*, **25**, 203–225.